

SMA Observations of Haro 2: Molecular Gas around a Hot Superbubble

SARA C. BECK,¹ PEI-YING HSIEH,² AND JEAN TURNER³

¹*School of Physics and Astronomy, Tel Aviv University, Ramat Aviv, Israel*

²*Academia Sinica, Institute of Astronomy and Astrophysics, P.O. Box 23-141, Taipei 10617, Taiwan*

³*Department of Physics and Astronomy, UCLA, Los Angeles, CA 90095-1547*

(Accepted MNRAS 2020 March 2)

ABSTRACT

Haro 2, a nearby dwarf starburst dwarf galaxy with strong Ly α emission, hosts a starburst that has created outflows and filaments. The clear evidence for galactic outflow makes it an ideal candidate for studying the role of molecular gas in feedback processes in a dwarf galaxy. We observed CO(2-1) in Haro 2 at the Submillimeter Array in the compact and extended configurations, and have mapped the molecular emission with velocity resolution 4.1 km s^{-1} and spatial resolution $2.0 \times 1.6''$. With this significant increase of resolution over previous measurements we see that the molecular gas comprises two components: bright clumps associated with the embedded star clusters of the starburst, and fainter extended emission east of the starburst region. The extended emission coincides with an X-ray bubble and has the kinematic signatures of an outflowing cone or of an expanding shell or bubble; the velocity range is $\sim 35 \text{ km s}^{-1}$. We suggest that the starburst winds that created the X-Ray bubble have entrained molecular gas, and that the apparent velocity gradient at an angle to the photometric axis is an artifact caused by the outflow. The molecular and X-ray activity is on the east of the galaxy and the ionized outflow and optical filaments are west; their relationship is not clear.

Keywords: galaxies:individual (Haro2), galaxies: kinematics and dynamics, galaxies: starburst

1. INTRODUCTION

Blue compact dwarf (BCD) galaxies form stars in environments quite different from gas-rich spirals or luminous infrared galaxies. BCDs are often rich in atomic gas but it is difficult to study their molecular components; the CO emission is usually weak and BCDs are often of low metallicity which complicates the interpretation of the emission. The origin of the molecular gas from which the stars are forming is thus unclear. Perhaps star-forming molecular clouds form from their reservoirs of atomic gas; alternatively, molecular gas could be acquired from other galaxies via accretion or merger. Another urgent question is how starburst feedback operates on molecular gas. The gravitational wells of dwarf galaxies are not as deep as spirals' and it is easier for them to lose gas to winds. However, molecular gas has greater cooling capacity than atomic, which can cause galactic winds to fail and inhibit gas dispersal. This can have ramifications for the escape of ionizing radiation from the starburst.

Haro 2 (Mrk 33, Arp 233, UGC 5720) is one of the best local targets in which to study the processes of star formation fueling and feedback in a dwarf galaxy. One of the most luminous BCDs, Haro 2 has a very blue nucleus (Haro 1956) is of moderate metallicity ($Z \sim Z_{\odot}/3$), with strong ultraviolet and optical emission lines and WR features (Kunth & Joubert 1985; Loose & Thuan 1986; Kinney et al. 1993), and bright radio continuum emission (Beck et al. 2000; Aversa et al. 2011), indicating very recent ($< 10 \text{ Myr}$) star formation. Haro 2 is one of the closest Lyman α emitting galaxies; Its strong, blue-shifted Ly α line is probably due to a outflow of ionized gas at $\approx 200 \text{ km s}^{-1}$ with respect to the galaxy (Lequeux et al. 1995; Meier et al. 2001). The ionized outflow is presumably driven by the massive stars in the starburst. Summers et al. (2001) observed the soft X-ray emission of Haro 2 with HRI on ROSAT with $1.5''$ pixels and saw “an extended, complex shell-like morphology”; they found hard emission concentrated in three point

sources as well as the widely distributed soft emission. CO(1–0), CO(2–1), and CO(3–2) lines have been detected with single dishes (Arnault et al. 1988; Sage et al. 1992; Barone et al. 2000; Meier et al. 2001; Mao et al. 2010; Israel et al. 1995). Haro 2 is comparatively weak in low J lines of CO relative to the brightness of the starburst, which is common for BCDs.

With sensitive array observations, CO can be mapped at the scales of individual giant molecular clouds (GMCs) in nearby galaxies, allowing the star formation process to be studied at the cluster scale. The first interferometric maps of CO and HI in Haro 2 were by Bravo-Alfaro et al. (2004); their map of CO(1–0) revealed unusual halo-like emission around the galaxy. They found the molecular gas to have a velocity gradient almost due north-south, at an angle $\sim 40^\circ$ to the photometric major axis of the galaxy, and suggested that the photometric and kinematic axes are misaligned.

This motivated us to observe Haro 2 in a higher transition; CO lines from high J are often stronger than CO(1–0) in BCDs, especially in regions of star formation (Israel et al. 1995; Meier et al. 2001). We accordingly observed Haro 2 in the CO(2–1) line with the Submillimeter Array (SMA) on Mauna Kea in both the extended and compact configurations, giving spatial resolution better than $2''$ and velocity resolution of $\approx 4 \text{ km s}^{-1}$ over the star forming region (observational parameters are in Table 1). We combine this data cube with archival radio continuum and optical images for a full picture of molecular gas kinematics in the center of Haro 2 which is very different from the earlier results.

2. OBSERVATIONS

We observed the CO(2–1) line in both the extended and compact configurations of the Submillimeter Array (SMA). The compact configuration, which has a maximum baseline of 70 m, was used on 13/6/2015 and the extended configuration with maximum baseline 220 m on 19/4/2016. Callisto was the absolute flux calibrator. Full parameters of the observations and the range of spatial resolutions achieved are in Table 1. The data was calibrated in MIRIAD and imaged with AIPS and CASA 4.7.0. Combining the extended and the compact configuration data created a data cube with spatial beam of $1.96 \times 1.61''$, almost as high as the extended configuration, but as sensitive as the compact configuration to large-scale structures; the largest structure that can be mapped is $\sim 210''$, corresponding to 22 kpc at the galaxy’s distance of 21 Mpc. Final noise levels in the individual combined channel maps are 17 mJy bm^{-1} . The integrated intensity (moment 0) image was constructed from all channels stronger than $> 1.5\sigma$. The intensity weighted mean velocity and dispersion maps (first and second moments) were constructed from emission $> 4\sigma$. Barone et al. (2000) obtained a peak $I_{\text{co}} = 7.6 \pm 0.3 \text{ K km s}^{-1}$ for Haro 2 at the IRAM 30-m telescope, which gives a total flux density of $\approx 84\text{--}125 \text{ Jy km s}^{-1}$, depending on the true source size. The SMA observations find a total flux $S(\text{CO}(2-1))$ of 110 Jy km s^{-1} , consistent with the single-dish measurements as far as can be determined.

3. SMA OBSERVATIONS OF CO(2–1): DISTRIBUTION OF EMISSION WITHIN HARO 2

3.1. Basic Structure: Starburst Clumps and an Extended Northeast Wing

The CO(2–1) total integrated intensity map of Haro 2 is displayed in Figure 1, as contours on an 814nm HST image. The total extent of the CO emission is about 1.5–2 kpc, about the size of the optical image. The brightest CO coincides with the brightest starburst region and there is extended CO emission east and north of the starburst. The edges of the extended CO lie near weak dust lanes, indicating that the extended CO is on the near side of the galaxy. These features are also seen in the CO(1–0) images of Bravo-Alfaro et al. (2004). We do not see CO(2–1) west of the starburst nucleus where Méndez & Esteban (2000) found $H\alpha$ filaments.

The CO(2–1) flux, S_{21} , is distributed with $\approx 50 \text{ Jy km s}^{-1}$ in the central starburst region and $50\text{--}60 \text{ Jy km s}^{-1}$ in the extended north-east emission. Bravo-Alfaro et al. (2004) find a CO(1–0) flux, S_{10} , of $\approx 17.6 \text{ Jy km s}^{-1}$ in the central region and $6\text{--}7 \text{ Jy km s}^{-1}$ in the extended. The S_{21}/S_{10} ratio of 2.9 in the central region is typical of compact galaxies (Israel, 2005) and thermally excited gas at $T \approx 10 \text{ K}$. The S_{21}/S_{10} flux ratio of the extended blue emission is 7–9, but this ratio simply reflects the fact that the CO(1–0) emission falls below the 1σ intensity cut of the CO(1–0) map at $100 \text{ mJy/bm km s}^{-1}$. This corresponds, for a typical S_{21}/S_{10} ratio of 3, to an rms almost 5 times higher than the $\approx 65 \text{ mJy/bm km s}^{-1}$ of our more sensitive maps. We do not expect to see the extended blue emission detected by the SMA in the Bravo-Alfaro et al. (2004) maps.

We can estimate the total mass in the extended emission from the observed $50\text{--}60 \text{ Jy km s}^{-1}$ by assuming $S_{21}/S_{10} \approx 3$ and X_{CO} , the conversion factor giving M_{H_2} from CO flux. For Bravo-Alfaro et al. (2004)’s X_{CO}

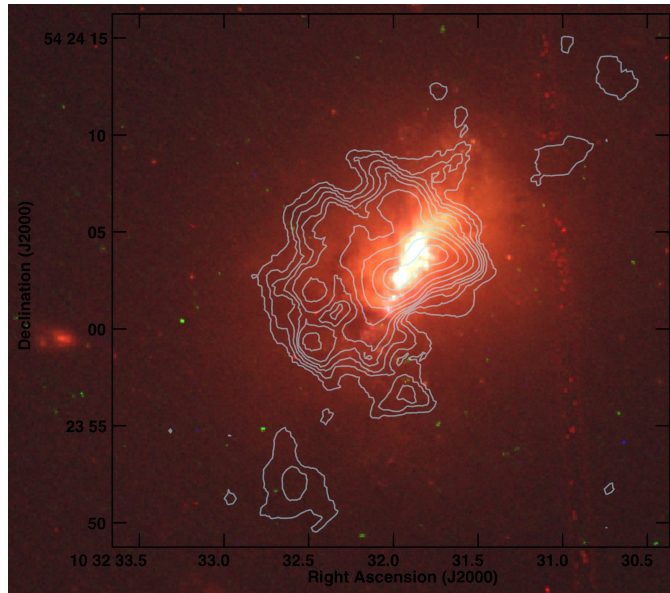


Figure 1. Zero moment (total intensity) map of the CO(2-1) emission in Haro 2 in contours, superimposed on an 814nm image from the Hubble Legacy Archive. The contour interval is 1800, starting at 1250; units are (Jy/bm)(m/s). The alignment of the images is estimated to be within $0.5''$.

value of $2 \times 10^{20} \text{ cm}^{-2} (\text{K km s}^{-1})^{-1}$, there is $5 \times 10^7 M_{\odot}$ in the extended emission region, and $1 \times 10^8 M_{\odot}$ for $X_{\text{CO}} = 4 \times 10^{20} \text{ cm}^{-2} (\text{K km s}^{-1})^{-1}$.

Figure 3 compares the CO(1-0) and CO(2-1) maps and shows the CO(2-1) extending north and east of the CO(1-0) emission. This will be discussed further in relation to the X-ray emission below.

Bravo-Alfaro et al. (2004) report ‘possible’ CO(1-0) concentrations south and northwest of the main emission region in a map made with a $3.3 \times 2.6''$ beam. These features are very weak at the full spatial resolution; tapering the beam to $\approx 3''$ shows emission at the $2 - 4\sigma$ per beam level northwest and south east of the main galaxy. These possible features appear in the moment maps of Figure 5. We believe them to be real, especially the extended northwest feature which covers several beams, but the signal-to-noise at this time is too low for meaningful study and they will not be discussed further here.

The starburst in Haro 2 has been mapped in the radio continuum by Beck et al. (2000) and Aversa et al. (2011) with beams of $2''$ and $1''$ respectively; at this resolution the emission appears as two bright regions. An archival VLA image from the AY35 program, shown in Figure 2, has resolution $0.58 \times 0.47''$ and shows that each of the bright regions breaks up into a few clumps. Figure 2 shows the CO(2-1) moment 0 overlaid with the high resolution radio map and demonstrates that the strongest CO emission mostly coincides with the two bright starburst clumps. In the right panel of Figure 2 we display the radio continuum and the $1.6 \mu\text{m}$ continuum mapped by NICMOS ¹

4. SMA OBSERVATIONS: THE KINEMATICS OF THE MOLECULAR GAS

The kinematics of gas in Haro 2 are of particular interest because it is one of the closest Lyman α emitting galaxies. Since Haro 2 does not have a particularly low metallicity, it has been suggested (Lequeux et al. 1995) that the escape of Lyman continuum photons is due to gas kinematics, and indeed there is a suggestion of outflow in the ionized gas (Legrand et al. 1997). How this might compare to the kinematics of the molecular gas is an important question. Furthermore, previous observations have found signs of unusual and non-rotational kinematics in Haro 2. Bravo-Alfaro et al. (2004) and Bravo-Alfaro et al. (2006) report that in both HI and CO the photometric and kinematic axes appear to be misaligned, with little velocity gradient along the major axis and a strong gradient at an angle of $\sim 40^\circ$ to it; similar results are reported for H α by Petrosian et al. (2002). These results have been taken as signs of a past accretion or merger event (Bravo-Alfaro et al. (2004) and Bravo-Alfaro et al. (2006)) However, the CO

¹ As astrometry from the NICMOS headers is known to be imprecise at the $1-2''$ level (Oti-Floranes et al. 2012), we shifted the NICMOS image $\sim 0.5''$ north-east to bring the strong southern infrared source into coincidence with the bright radio clump.

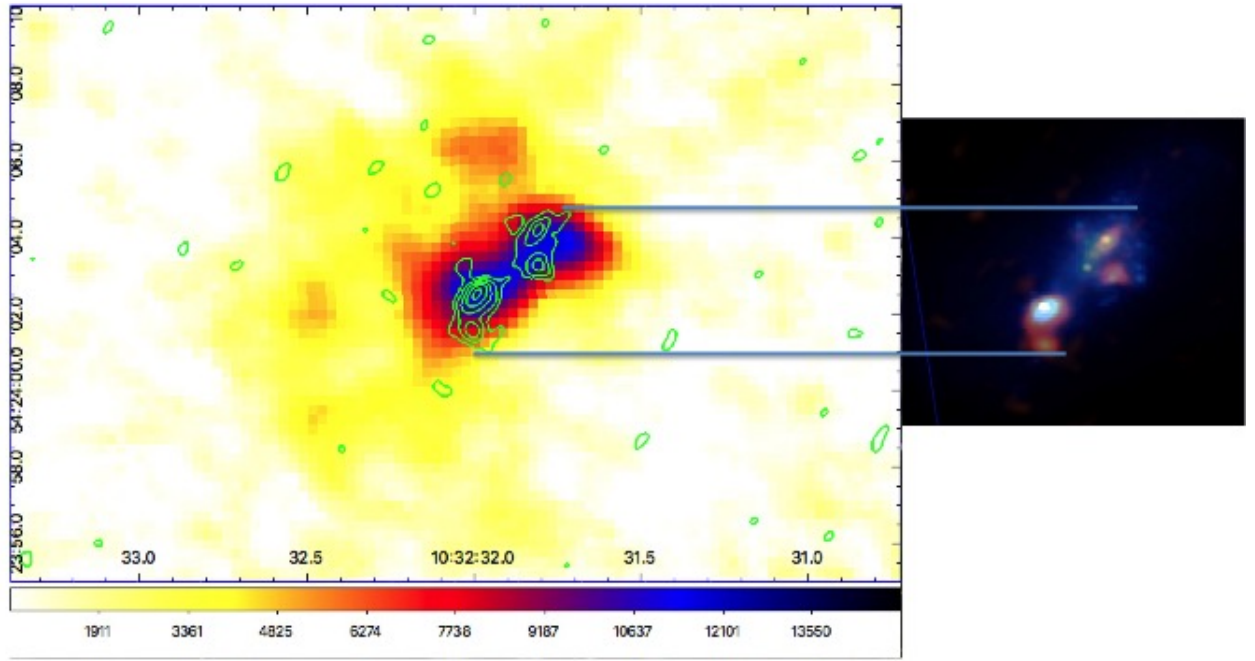


Figure 2. The CO(2-1), radio and near-infrared emission of Haro 2. The left panel displays the integrated intensity (moment 0) of CO(2-1) in color, with the 6 cm radio continuum overlaid in green contours. The color wedge units are Jy/bm m/s and contours are multiples of 1.5×10^{-4} Jy/bm from the base of 2.5×10^{-4} Jy/bm. The left panel is cropped to the region of star-forming clumps as marked by the lines and shows the 6 cm radio continuum in red and the $1.6 \mu\text{m}$ emission (from NICMOS) in blue.

data cube on which these arguments were based only covered velocities of 1378 to 1503 km s^{-1} and had beam size $3.2 \times 2.6''$. The SMA data with its better spatial resolution and more complete velocity coverage presents a somewhat different picture, which we now discuss.

Figure 4 displays samples of channel maps of CO(2-1) emission (a complete set of channel maps is in the Appendix). The CO(2-1) emission in Haro 2 spans a total velocity range of $\approx 200 \text{ km s}^{-1}$ FWZI, from about 1380 to 1580 km s^{-1} , with a centroid of 1470 km s^{-1} (Bravo-Alfaro et al. (2004) found 1440 km s^{-1} as the center of the HI line). Figure 5 displays the first moment (intensity-weighted peak velocity) and second moment (dispersion) of the CO(2-1) line, with the radio continuum contours superimposed to show the location of the young star clusters and the photometric axis of the galaxy. These displays of the kinematics show:

- Along the axis defined by the positions of the young star clusters there is a smooth velocity gradient from $\approx 1465 \text{ km s}^{-1}$ on the north to $\approx 1510 \text{ km s}^{-1}$ on the south.
- The extended emission north and east of the starburst is blue-shifted relative to the starburst and has velocities between $\approx 1420 \text{ km s}^{-1}$ and $\approx 1460 \text{ km s}^{-1}$.
- The velocity field of the extended blue emission is complex.

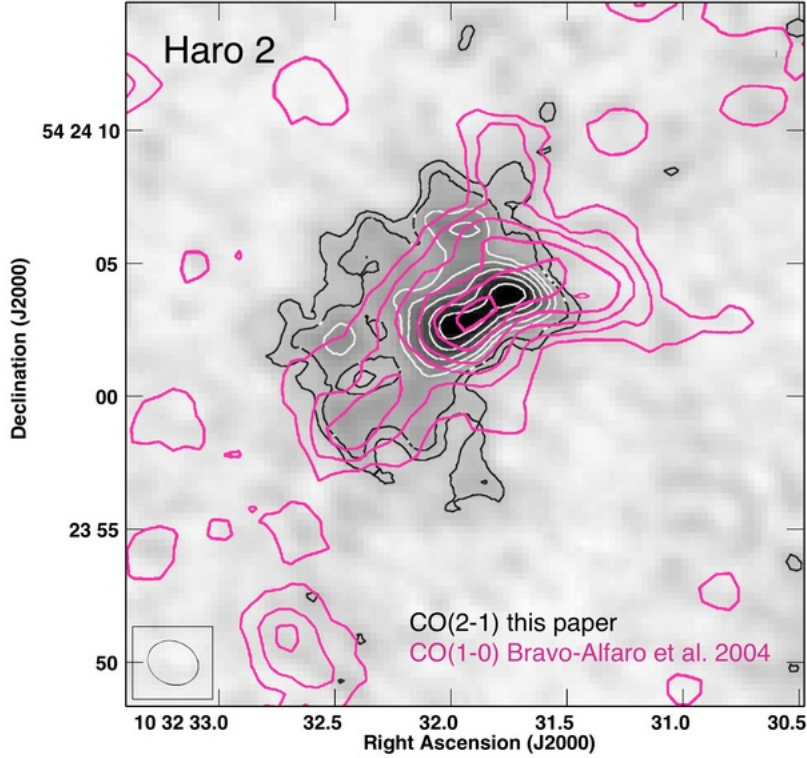


Figure 3. The CO(2-1) emission in grayscale and black and white contours together with the (1-0) emission from Bravo-Alfaro et al. (2004) in colored contours. The (2-1) is enhanced relative to the (1-0) north and east of the starburst region.

- Over most of the region of extended blue emission the dispersion is high.

We conclude that the galaxy holds two distinct kinematic regions: the starburst lying along the photometric axis, and the blue emission north-east of the main body of the galaxy. We now discuss each component.

4.1. Molecular Gas Kinematics in the Starburst

The channel maps of Figure 3 clearly show two velocity components associated with the starburst: one at $\sim 1510 \text{ km s}^{-1}$ on the southeast star-forming clump and another component at $\sim 1470 \text{ km s}^{-1}$ on the north clump, giving a centroid of 1490 km s^{-1} . How do these velocities compare to those seen at optical wavelengths? The $H\alpha$ spectra of Méndez & Esteban (2000) found velocities of ≈ 1430 , ≈ 1450 and ≈ 1465 on their $H\alpha$ knots 1,2,3 respectively. They do not give absolute coordinates for their positions, but from their offsets and by comparing the $H\alpha$ image to the near-infrared, we conclude that their $H\alpha$ knots 1 and 2 are north of the radio emission region and *not* associated with the star forming clumps. Their knot 3 corresponds to the the northern radio source and agrees with it in velocity. That the southern radio source has no associated $H\alpha$ is a sign of high local extinction, which plays an important role in the appearance of this galaxy's core.

The central panel of Figure 6 shows the velocity as a function of position (Position-Velocity Diagram of PVD) along the main body of the galaxy as defined by the radio clumps. The velocity shift between the two sources is consistent with the gradient set by the $H\alpha$ clumps, further north along the same axis. The patch of high dispersion

with $\sigma \approx 35 \text{ km s}^{-1}$ that appears in Figure 5 between the two radio concentrations shows where emission of both groups of sources enter the beam.

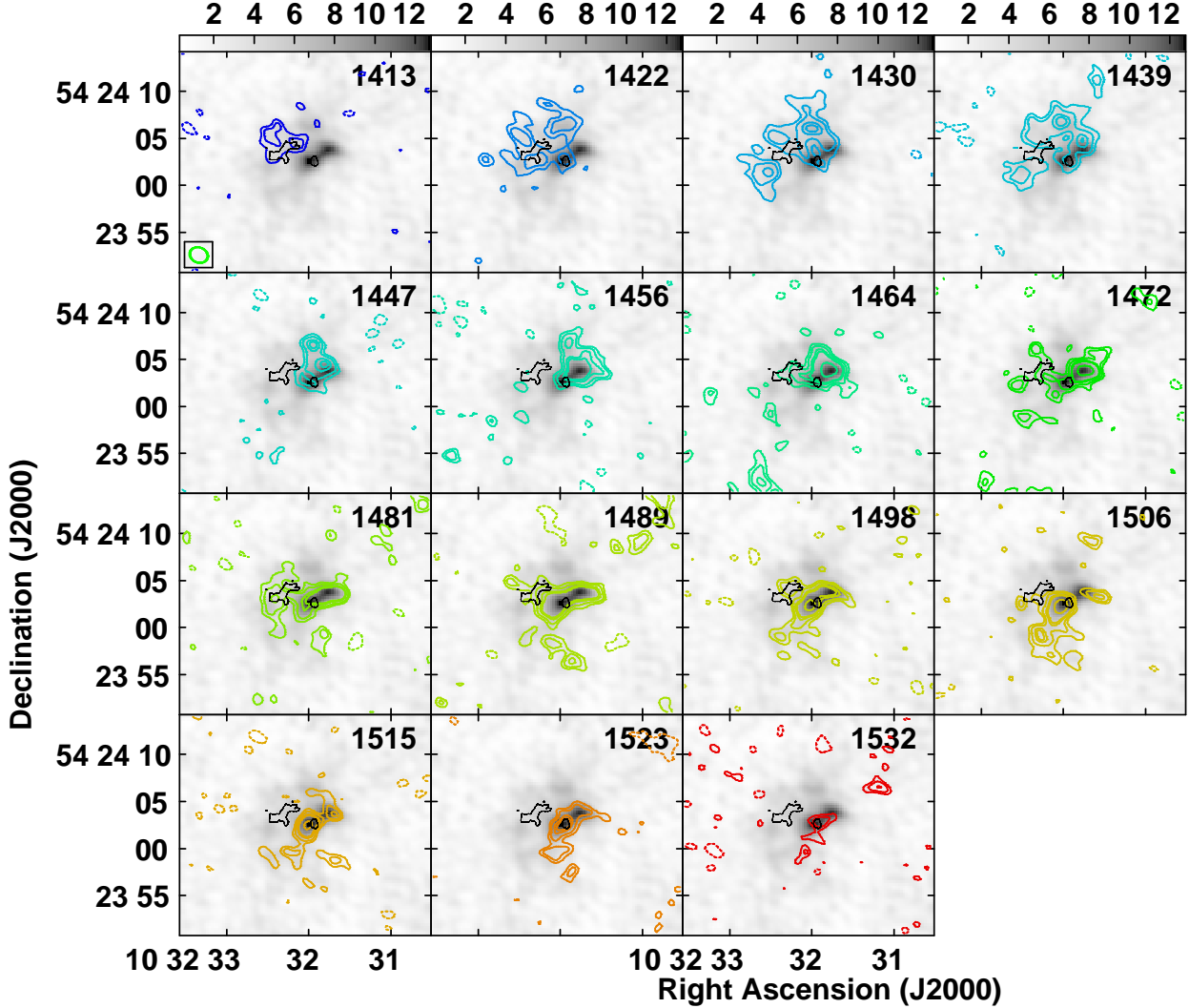


Figure 4. Contours of the CO(2-1) line emission in a 4 km s^{-1} channel at the velocity shown in each panel, overlaid on the total intensity map in greyscale. Panels are labelled by velocity and contour levels are $4 \times 10^{-2} \times 2^{n/2} \text{ Jy/bm}$. Every other channel in the range of strongest emission are shown here; the full set is in the Appendix. The thin black contour in each panel is the contour of highest velocity dispersion shown in Figure 5.

4.2. Molecular Gas North East of the Starburst: A CO Outflow or Expanding Bubble

The emission north-east of the starburst extends over $\sim 1.5\text{-}2 \text{ kpc}$ and $1400\text{-}1500 \text{ km s}^{-1}$ in velocity. The first and second moment maps of Figure 5 and the channel maps in Figure 4 and the Appendix show that the extended eastern emission is entirely blue of the main starburst; the blue velocities of the extended eastern emission have no counterpart in the optical spectra. The eastern emission is concentrated at two velocities $\approx 45 \text{ km s}^{-1}$ apart; these appear in the channel maps of Figure 4 as two ‘horns’ extending east from the starburst region. These features appear clearly in Position-Velocity Diagrams (PVDs) in Figure 6. In short, the channel maps, PVD and line profiles of the molecular gas east of the starburst all demonstrate the kinematic signatures of a body of gas flowing away from the galaxy with velocity $\sim 35 - 45 \text{ km s}^{-1}$.

Two types of motions that could produce this kinematic signatures are 1) an expanding shell or bubble, 2) outflow cones based in the starburst. In a true bubble expanding from a central point, the highest velocities and the greatest

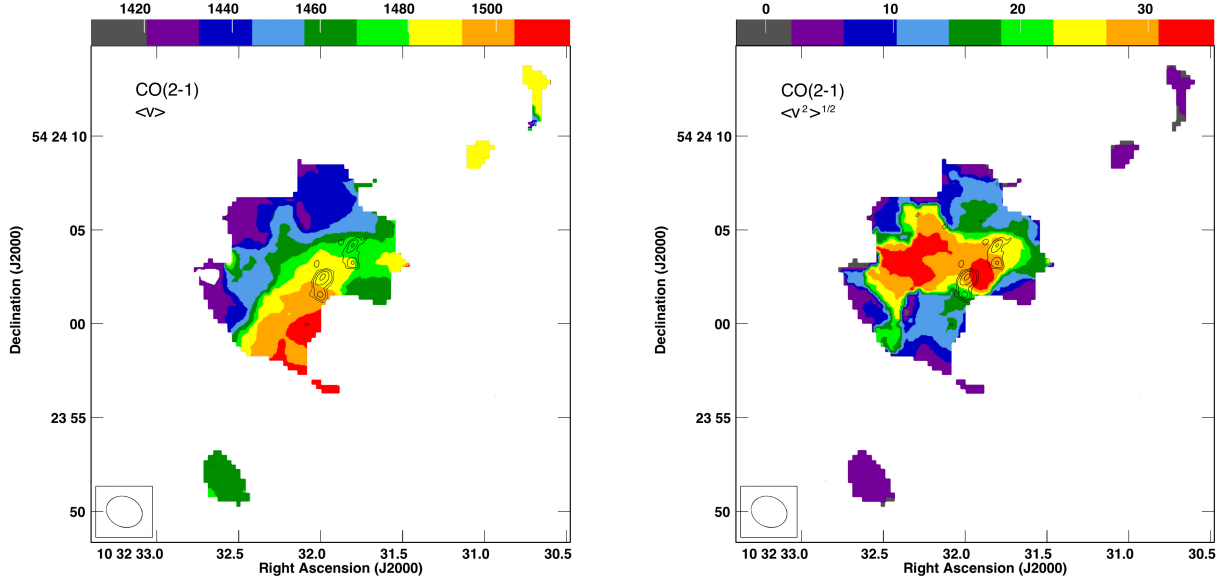


Figure 5. Intensity-weighted mean velocity (left) and velocity dispersion (right) of CO(2–1) in Haro 2. The units of the color wedges are km s^{-1} . The radio contours of Figure 2 are superimposed on the moment maps.

velocity dispersion will be seen in the center. In the Haro 2 extended emission region the most extreme gas velocities and the region of highest velocity dispersion, shown as a thin black contour on the channel maps, are not in the center of the emission but closer to the starburst. This may argue that the blue velocities show outflows from the clusters. However, the gas spatial distribution is patchy and if there is a shell it is very incomplete and difficult to see. It may not be possible with the current data to distinguish clearly between expansion of a partial shell and an set of outflows. We refer below to this component of molecular gas as a ‘bubble’ because it coincides with a well-known X-ray bubble, with the caveat that the molecular gas may not have identical morphology.

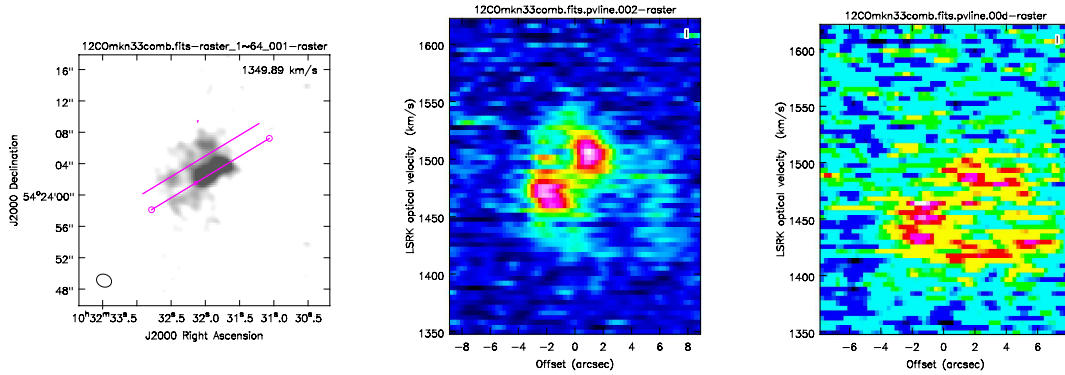


Figure 6. Position-Velocity diagrams of the CO(2–1) emission. The left panel shows the slices on which the velocities were measured, overlaid on the moment 0 total emission map in grayscale. The middle panel is the PVD on the lower line, through the main clusters, and the right panel is the PVD on the upper line through the bubble. Negative offsets are east.

4.2.1. The Molecular Outflow and the X-Ray Emission

The large-scale activity reflected in the molecular outflow appears as well in the high energy regime. [Summers et al. \(2001\)](#) observed Haro 2 with HRI on ROSAT with a $\sim 5''$ beam and $1.5''$ pixels and saw “an extended, complex shell-like morphology”. [Oti-Flóranes et al. \(2012\)](#) observed with CHANDRA over a wider energy range and with $0.49''$ pixels. Their image of the soft (0.2–1.5 KeV) emission is very similar to the ROSAT result; they find in addition 3 point-like sources of hard (2.5–8.0 KeV) X-rays. How does the structure correspond to the molecular gas? In Figure

8 we overlay the CO(2-1) map on the full resolution ROSAT X-ray image. The CO(2-1) line agrees well with the soft X-ray distribution: the X-ray shell coincides with the blue CO emission and the base of the shell with the starburst clusters.

Oti-Floranes et al. (2012)’s dominant hard x-ray source, X1, agrees with the brightest near-infrared clump in NICMOS images. We identify the near-infrared peak with the brighter (northern) sub-clump in the southern starburst region of Figure 2, although the formal coordinates disagree by about $1''$; Oti-Floranes et al. (2012) also note this inconsistency in the coordinates. With this alignment, the secondary hard X-ray source X2 agrees with the weaker southern sub-clump. We do not have a candidate for the X3 source that Oti-Floranes et al. (2012) suggest may not belong to the galaxy.

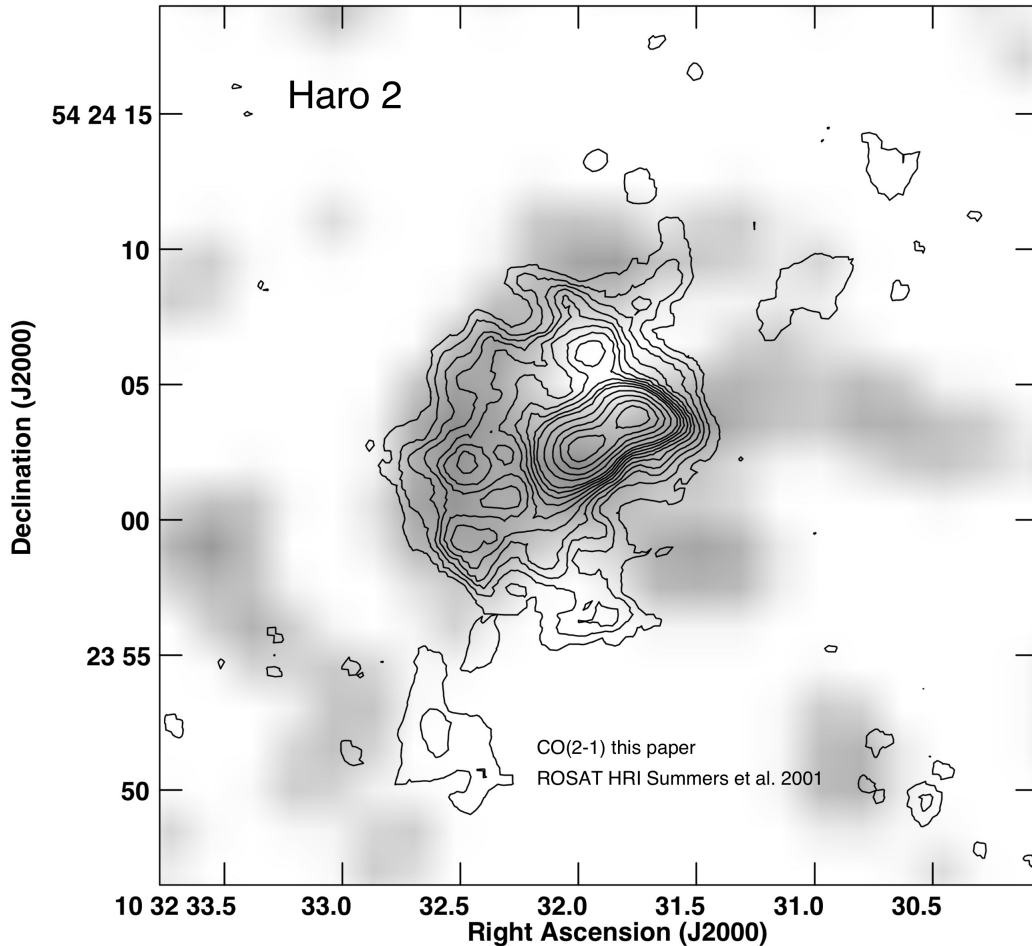


Figure 7. The X-ray emission from the map of Summers et al. (2001) in grayscale and the integrated CO(2-1) emission in contours. Contour levels are $n \times 600$ mJy/bm km/s for $n = 1 - 10$ and $n \times 1200$ mJy/bm km/s for n greater than 10.

The CO(2-1) agrees spatially with the X-ray better than does the CO(1-0); Bravo-Alfaro et al. (2004) show in their Figure 8 that the X-ray extends further to the east than does the CO(1-0) emission. That the CO(2-1) is a better match than the (1-0) with the X-ray may be partly due to the improved sensitivity of the CO(2-1) but also because the gas is warm or hot: a jiggle-mode maps of CO(3-2) with $14.5''$ resolution in the JCMT Nearby Galaxies Legacy Survey (Wilson et al. 2012) shows (their figure C26) the CO(3-2) emission clearly extended north and east of the optical nucleus, consistent with the CO(2-1) appearance. That the higher CO transitions are consistently stronger than the (1-0) east of the galaxy implies that the eastern gas is warm and the upper levels populated, as is seen near other strong starbursts (Consiglio et al 2016). We conclude that the extended blue molecular gas, be it bubble or outflow, is associated with the hot X-ray emitting gas. The double velocity peaks of the CO line here resembles

that on an X-ray source in He 2-10, (Beck et al. 2018) and CO lines are seen emitted from the edges of other bubbles and superbubbles (e.g. Matsushita et al (2005), Sano et al (2017), Tsai et al (2009)). The molecular gas is probably concentrated in the thin, dense shell created in the ‘snowplow’ stage (Summers et al. 2001). We estimate the total energy in the outflowing molecular gas from its mass of $\approx 1 \times 10^8 M_\odot$ (derived with $X_{\text{CO}} = 4 \times 10^{20} \text{ cm}^{-2} (\text{K km s}^{-1})^{-1}$) and a typical 35 km s^{-1} velocity to be $\approx 10^{54}$ ergs, again similar to He 2-10.

4.2.2. Kinematics of the X-Ray Bubble, Molecular Gas and $H\alpha$

Summers et al. (2001) model their X-ray bubble as resulting from the stellar winds of the nuclear starburst under the assumption that it is the same process as the ionized outflow observed in $H\alpha$. They accordingly use the size and expansion velocity Legrand et al. (1997) found for the $H\alpha$ system to determine parameters of the the X-ray bubble. But the current data show clearly that the X-ray and molecular bubble is *east* of the nucleus. Although the spectra of Legrand et al. (1997) cannot be registered spatially because of the very poor seeing, it is reasonable to associate the ionized outflow they observe in $H\alpha$ with the $H\alpha$ filaments seen in the deep images of Méndez & Esteban (2000) *west* of the nucleus. The velocities are another discrepancy between the ionized and molecular kinematics: the ionized outflow has expansion velocity $\sim 200 \text{ km s}^{-1}$, significantly higher than the $\sim 40 \text{ km s}^{-1}$ of the molecular velocities.

We conclude that the nuclear region of Haro 2 drives *two* outflows: to the west, a fast ionized outflow which has created $H\alpha$ filaments, and to the east a bubble of hot, X-ray emitting gas which has entrained warm molecular gas.

How will the results calculated by Summers et al. (2001) change in this model? The important difference is that the expansion velocity may have been overestimated. If the observed molecular velocities of $\sim 40 \text{ km s}^{-1}$ are used, instead of the 200 km s^{-1} found from the $H\alpha$ results, for v_b in their Equation 8, the age estimate is 1.8×10^7 yr, instead of 3.2×10^6 yr. The longer time is more consistent than the short with other estimates of the age of the relatively mature starburst of Haro 2. The longer lifetime in turn reduces the mechanical injection power derived; Summers et al. (2001)’s Equation 1 gives $1.35 \times 10^{39} \text{ erg s}^{-1}$ instead of $2.4 \times 10^{41} \text{ erg s}^{-1}$. Such energy can be readily supplied by the stellar population of any one of the nuclear clumps. The most likely driver is in the northern source, as its velocity overlaps with velocities in the CO bubble.

4.2.3. Re-evaluating the Global Kinematics of Haro 2

Identifying the blue-shifted molecular gas NE of the galaxy as an outflow means that we must re-appraise the overall CO and HI kinematics described by Bravo-Alfaro et al. (2004). While the blue-shifted holds only $\sim 1/2$ of the total gas mass, it is so spatially distinct that it appears clearly in first moment maps and create an apparent velocity gradient NE to SW, at an angle to the optical major axis. We believe this is what Bravo-Alfaro et al. (2004) see in their HI data as well. Now that we treat the blue CO emission as a separate feature, a bubble driven by the northern star clusters, the only velocity gradient is along the photometric major axis.

Is the CO and X-ray bubble the base of a true galactic wind; in other words, will the matter in the bubble escape from the galaxy? We do not have a model for the mass distribution of Haro 2 but can make a first estimate by treating it as an dE type; escape velocity from a dE galaxy of Haro 2’s luminosity is expected to be $\approx 80 \pm 15 \text{ km s}^{-1}$ (Merritt et al. (2004), Figure 2). If this approximation is valid to within a factor of 2, it would indicate that only the very fastest gas may escape from the galaxy, while the bulk of the molecular gas will enter new orbits or fall back onto the galaxy core.

5. SUMMARY AND DISCUSSION

We report observations of CO (2-1) in Haro 2 which combine the SMA in extended and compact arrays to give beam sizes $\approx 2 - 7''$. The major findings are:

- Approximately 1/2 the molecular gas is in two clumps, kinematically and spatially distinct and coincident with the bright radio sources which are identified as obscured starburst clumps.
- Approximately 1/2 of the molecular gas is in a blue-shifted outflow or bubble north-east of the galactic nucleus, with expansion velocity $\sim 35 - 40 \text{ km s}^{-1}$.
- The blue CO outflow coincides with an X-ray superbubble which is believed to have been created by stellar winds in the starburst, and with no other known sources. The molecular gas has probably been entrained by the hot gas in the outflows.

- The reported misalignment of the optical and kinetic axis in Haro 2 now appears to be an artifact caused by low spatial resolution of earlier observations.

It is not clear how the stellar activity that created the molecular bubble is related to the ionized outflow and $H\alpha$ filaments seen west of the galaxy by Méndez & Esteban (2000). Is one starburst clump driving two outflows of different types in different directions? Are the ionized and molecular outflows driven by two different sources? Is there an ionized outflow connected to the molecules and X-rays that has not yet been detected? It would be very useful to observe Haro 2 further in optical emission lines to determine the full extent of its outflow activity, and in higher transitions of CO to determine conditions in the molecular clouds associated with the X-ray superbubble.

SCB thanks You-Hua Chu for helpful discussions and ASIAA for hospitality during this work.

Facilities: SMA

Software: CASA, AIPS, ds9

REFERENCES

- Arnault, P., Casoli, F., Combes, F., et al. 1988, A&A, 205, 41
- Aversa, A. G., Johnson, K. E., Brogan, C. L., Goss, W. M., & Pisano, D. J. 2011, AJ, 11996ApJ...460..271K41, 125
- Barone, L. T.; Heithausen, A.; Huttemeister, S.; Fritz, T.; & Klein, U., MNRAS, 317, 649
- Beck, S. C., Turner, J. L., & Kovo, O. 2000, AJ, 120, 244
- Beck, S.C., Turner, Jean L. & Consiglio, S.Michelle 2018, ApJ, 867, 165
- Bravo-Alfaro, H., Brinks, E., Baker, A. J., Walter, F., & Kunth, D. 2004, AJ, 127, 264
- Bravo-Alfaro, H., Coziol, R., & Brinks, E. 2006, RMxAA, 42, 261
- Consiglio, S. Michelle; Turner, Jean L.; Beck, Sara; & Meier, David S., 2016, ApJL, 833, L6
- Haro, G. 1956, Boletín de los Observatorios Tonantzintla y Tacubaya, 2, 8
- Israel, F. P., Tacconi, L. J., & Baas, F. 1995, A&A, 295, 599
- Israel, F.P., 2005, A&A438, 8551
- Kinney, A. L., Bohlin, R. C., Calzetti, D., Panagia, N., & Wyse, R. F. G. 1993, ApJS, 86, 5
- Knapp, G. & Rupen, M. , 1996,1988ApJ...333..821M ApJ460, 271
- Kobulnicky, Henry A., & Gebhardt, Karl 2000, AJ, 119, 119
- Kunth, D., & Joubert, M. 1985, A&A, 142, 411
- Legrand, F., Kunth, D., Mas-Hesse, J. M., & Lequeux, J. 1997, A&A, 326, 929
- Lequeux, J., Kunth, D., Mas-Hesse, J. M., & Sargent, W. L. W. 1995, A&A, 301, 18
- Loose, H.-H., & Thuan, T. X. 1986, ApJ, 309, 59
- MacLaren, I., Richardson, K., & Wolfendale, A. ApJ, 333, 821 (1988)
- Mas-Hesse, J. M., & Kunth, D. 1999, A&A, 349, 765
- Mas-Hesse, J. M., Kunth, D., Tenorio-Tagle, G., et al. 2003, ApJ, 598, 858
- Mao, R.-Q., Schulz, A., Henkel, C., et al. 2010, ApJ, 724, 1336
- Matsushita, Satoki; Kawabe, Ryohei; Kohno, Kotaro; Matsumoto, Hironori; Tsuru, Takeshi G.; & Vila-Vilaro, Baltasar, 2005, ApJ618, 761
- Meier, D. S., Turner, J. L., Crosthwaite, L. P., & Beck, S. C. 2001, AJ, 121, 740
- Méndez, D. I., & Esteban, C. 2000, A&A, 359, 493
- Merritt, D., Milosavljevi?, M., Favata, M., Hughes, S., Holz, D. E. 2004, ApJL607, 9
- Murphy, E. J., Bremseth, J., Mason, B. S., et al. 2012, ApJ, 761, 97
- Oti-Floranes, H.; Mas-Hesse, J. M.; Jimenez-Bailon, E.; Schaefer, D.; Hayes, M.; Ostlin, G.; Atek, H.; Kunth, D. Petrosian, A. R., Movsessian, T., Comte, G., Kunth, D., & Dodonov, S. 2002, A&A, 391, 487
- Sage, L. J., Salzer, J. J., Loose, H.-H., et al. 1992, A&A, 265, 19
- Sano, H.; Yamane, Y.; Voisin, F.; Fujii, K.; Yoshiike, S.; Inaba, T.; Tsuge, K.; and 11 coauthors, 2017, ApJ843, S61
- Summers, L. K., Stevens, I. R., & Strickland, D. K. 2001, MNRAS, 327, 385
- Thuan, T., Hubbard, J., & Levrier, F. AJ, 128, 617 (2004)
- Tsai, An-Li, Matsushita, Satoki; Nakanishi, Kouichiro; Kohno, Kotaro; Kawabe, Ryohei; Inui, Tatsuya; Matsumoto, Hironori; Tsuru, Takeshi G.; Peck, Alison B.; & Tarchi, Andrea, 2009, PASJ61, 237
- Turner, J. L., & Ho, P. T. P. 1994, ApJ, 421, 122
- Wilson, C.D. and numerous co-authors 2012, MNRAS, 424, 3050

Table 1. Observational Parameters

Date	Telescope	Wavelength	Beam Size	Spectral Channels	noise Jy/bm
18/4/16	SMA-Extended	230 GHz	$1.25 \times 0.97''$	$65 \times 4.2 \text{ km s}^{-1}$	9×10^{-3}
04/01/16	SMA-Compact	"	$7.11 \times 4.55''$	"	1.9×10^{-2}
n.a.	SMA-Combined	"	$1.96 \times 1.61''$	"	1.7×10^{-2}
02/11/90	VLA-C array	4.86 GHz	$0.59 \times 0.47''$	n.a.	8.0×10^{-5}

6. APPENDIX

Kinematic Channel Maps

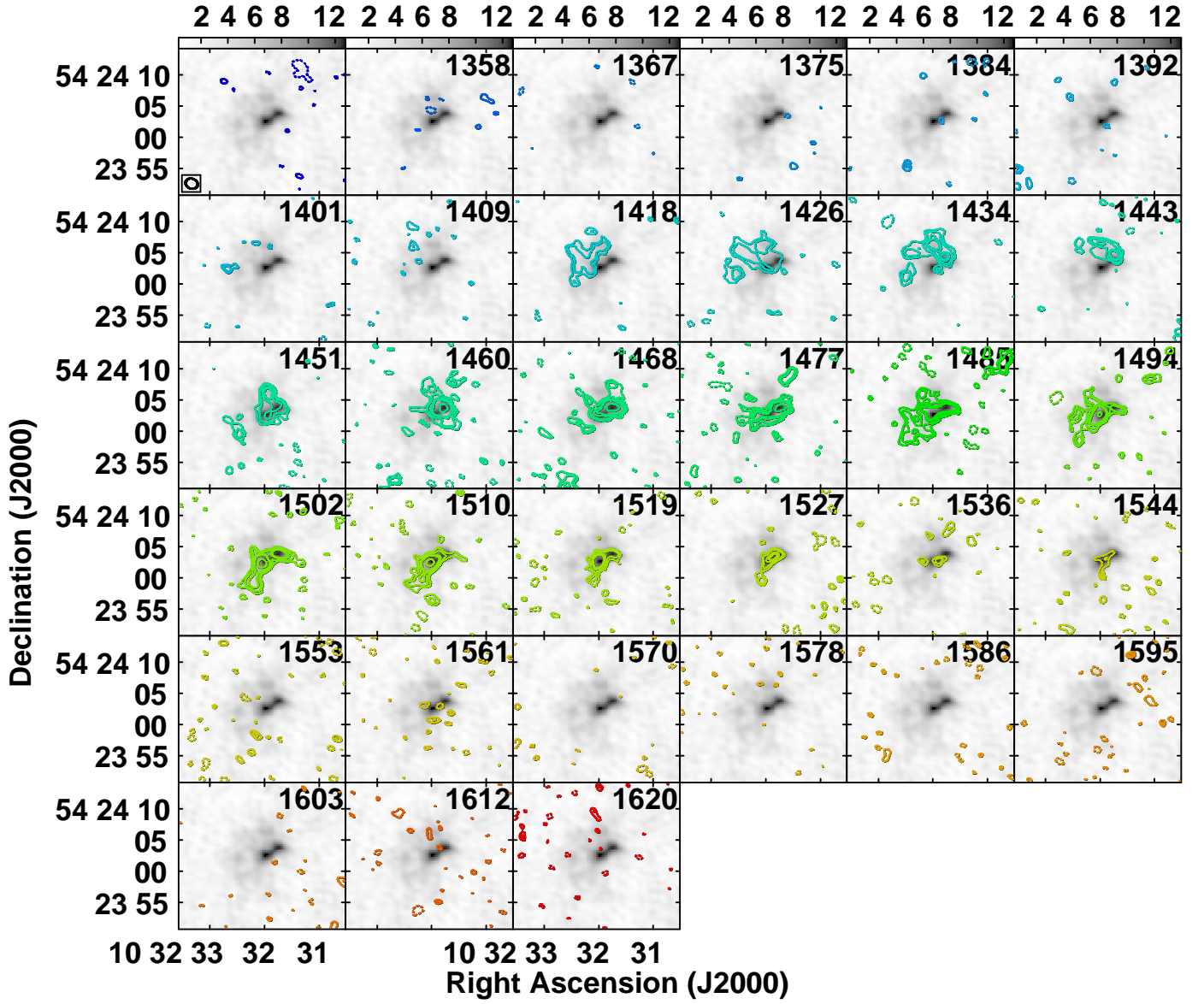


Figure 8. Velocity channel maps of Haro 2 showing all velocity channels, overlaid on the moment 0 total emission map. The contours are $4 \times 10^{-2} \times 2^{n/2}$ Jy/bm and the greyscale range is -0.25 to 12.37 (Jy/bm)(km s^{-1}).